The structure and stability of extended, inclined circumplanetary disc or ring systems

Jessica Speedie [1,2]★ and J. J. Zanazzi [1]★

[1] *Canadian Institute for Theoretical Astrophysics, University of Toronto, 60 St. George Street, Toronto, ON M5S 1A7, Canada*
[2] *School of Interdisciplinary Science, McMaster University Hamilton, ON L8S 4M1, Canada*

ABSTRACT

Large dips in the brightness for a number of stars have been observed, for which the tentative explanation is occultation of the star by a transiting circumplanetary disc or ring system. In order for the circumplanetary disc/rings to block the host star's light, the disc must be tilted out of the planet's orbital plane, which poses stability problems due to the radial extent of the disc required to explain the brightness dip durations. This work uses *N*-body integrations to study the structure and stability of circumplanetary disc/ring systems tilted out of the planet's orbital plane by the spinning planet's mass quadrupole. Simulating the disc as a collection of test particles with orbits initialized near the Laplace surface (equilibrium between tidal force from host star and force from planet's mass quadrupole), we find that many extended, inclined circumplanetary discs remain stable over the duration of the integrations ($\sim$ 3–16 Myr). Two dynamical resonances/instabilities excite the particle eccentricities and inclinations: the Lidov-Kozai effect which occurs in the disc's outer regions, and ivection resonance which occurs in the disc's inner regions. Our work places constraints on the maximum radial extent of inclined circumplanetary disc/ring systems, and shows that gaps present in circumplanetary discs do not necessarily imply the presence of exomoons.

Key words: planets and satellites: detection – planets and satellites: dynamical evolution and stability – planets and satellites: individual: J1407b – planets and satellites: rings – planet–disc interactions.

1 INTRODUCTION

The detection and characterization of circumplanetary discs and/or rings around giant planets may soon be at the frontier of exoplanetary science. If a giant planet is embedded in its natal protoplanetary disc, a young gaseous circumplanetary disc is most detectable from its near-infrared emission (Szulágyi et al. 2019), but may also be detectable from its continuum (Szulágyi et al. 2018) and polarized scattered light (Szulágyi & Garufi 2019) emission. Recently, a circumplanetary disc around the Jovian planet PDS 70b has been detected, inferred by the disc's excess infrared emission, and H α and Br γ line emission from accretion on to the planet (Christiaens et al. 2019).

For more evolved systems, one can detect discs/rings around transiting planets using photometry, when the rings transit before (after) the planet during ingress (egress) (e.g. Schneider 1999; Barnes & Fortney 2004; Ohta, Taruya & Suto 2009; Zuluaga et al. 2015; Rein & Ofir 2019; Sandford & Kipping 2019). Numerous searches for planetary rings have been conducted, and while most have been inconclusive (e.g. Brown et al. 2001; Heising, Marcy & Schlichting 2015; Santos et al. 2015), one possible detection of an exoring system has been made around the planet KIC 10403228 (Aizawa et al. 2017). These searches have targeted planets that may host rings orbiting out to distances a few times larger than the host planet's radius, similar to the rings around Saturn.

In contrast to these searches for relatively compact exoring systems, a number of tentative detections of more extended exoplanetary discs have been made around dipper stars. Dipper stars typically lie in young stellar associations (ages $\lesssim$ 100 Myr), and display periodic, quasi-periodic, or aperiodic brightness variations (along with many other stars in the cluster) which cannot be explained by intrinsic stellar activity, but are thought to be due to material in the surrounding environment blocking some of the star's flux. These stellar brightness dips have been attributed to many astrophysical phenomena, including occultations from dusty material near the inner edge of circumstellar discs (e.g. Cody et al. 2014; McGinnis et al. 2015; Ansdell et al. 2016; Hedges, Hodgkin & Kennedy 2018), transiting exocomets (e.g. Rappaport et al. 2018; Ansdell et al. 2019), and tidally disrupted discs from binary interactions (e.g. Rodriguez et al. 2018). Of interest for this work are the 'deep dipper' stars 1 SWASP J140747-354542 (Mamajek et al. 2012), PDS 110 (Osborn et al. 2017, 2019), VVV-WIT-07 (Saito et al. 2019), and EPIC 204376071 (Rappaport et al. 2019), with large ($\gtrsim$ 30–80 per cent) brightness dips. One proposed explanation for the deep dipper brightness fluctuations is a transit by a planet hosting an extended, optically thick circumplanetary[1] disc/ring[2] system. In order to explain the depth and

---

[1]Throughout this work, we will refer to these discs as circumplanetary, but note the secondaries' masses may be substellar ($\gtrsim$ 13 M_{Jup})
[2]We will refer to the structure surrounding the planet as a disc and/or ring system interchangably throughout this work

★ E-mail: jspeedie@cita.utoronto.ca (JS); jzanazzi@cita.utoronto.ca (JJZ)

duration of these large brightness decreases, the circumplanetary disc/ring system must extend out to distances comparable to the planet's Hill radius (e.g. Mamajek et al. 2012, see also Section 4.1).

The most studied of these deep dippers is the star 1 SWASP J140747-354542 (hereafter J1407). In 2012, Mamajek et al. (2012) presented photometry from the SuperWASP (Super Wide Angle Search for Planets) data base (Pecaut & Mamajek 2013) of J1407, a young (∼16 Myr old) K5 pre-main sequence star at ∼130 pc in the Sco-Cen OB Association. The star's light curve exhibited a complex series of deep eclipses that lasted ∼54 d around the month of 2007 April. The authors interpreted the light curve of J1407 as the transit of a circumplanetary disc surrounding an unseen substellar companion, J1407b. They fit the gross features of the nightly mean SuperWASP photometry with a simple ring model and proposed that we had detected one of the first circumplanetary discs outside our Solar system (Mamajek et al. 2012).

The J1407b system has since been the subject of a number of subsequent studies, which have refined the simple ring model to accurately fit the reduced light curve (Van Werkhoven, Kenworthy & Mamajek 2014; Kenworthy & Mamajek 2015), placed constraints on the mass and period of the companion (Kenworthy et al. 2014; Mentel et al. 2018), constrained the radial extent of the disc (Rieder & Kenworthy 2016), and explored whether the rapid flux variations in J1407's light curve can be attributed gaps opened by mean motion resonances with nearby moons (Sutton 2019). The best-fitting ring model presented in Mamajek et al. (2012) is flat, inclined with respect to the companion's orbital plane by 24.2°, and very extended, with an outer radius of $r_{out} \sim 0.6$ au.

While the J1407b circumplanetary disc hypothesis (along with PDS 110, VVV-WIT-07, and EPIC 204376071) remains unconfirmed (see Section 4.1 for a discussion), the question of the dynamical stability of extended circumplanetary discs is pertinent to the up-coming discovery of more exoring candidates. It is likely that our first detections will be of extended ring systems due to their larger transit signal. For exorings to produce a transit signal at all, the disc must be inclined with respect to the planet's orbital plane, and the rings must be stable to gravitational perturbations from the host star over the system's lifetime (e.g. Schlichting & Chang 2011; Zanazzi & Lai 2017a). Without any stabilizing forces, the gravitational influence of the host star will destroy the rings over a time-scale much shorter than the system's age (Sucerquia et al. 2017).

The rings and many satellites of the four giant planets in our Solar system are inclined with respect to the planets' orbital planes (and are aligned with the planets' equators) due to the fact that the planets are spinning and oblique. The competition between the interior quadrupole potential from a spinning planet's equatorial bulge and the external tidal potential from the host star determines an equilibrium surface surrounding the planet: the 'Laplace surface' (Laplace & Celeste 1805). In this work, we explore the dynamical stability of the Laplace surface around an oblate and oblique planet with N-body integrations, assuming the particles which compose the disc are massless. Our goal is to probe the stability of collisionless circumplanetary debris discs, applying our results to the tentative exoring systems already detected, with an eye towards constraining the properties of exoring systems which may be detected in the future. In Section 2, we describe our circumplanetary disc model in detail and outline how we perform our N-body integrations. We present our main results in Section 3, and discuss their implications in Section 4. Section 5 summarizes our results and draws our main conclusions.

2 SIMULATIONS

2.1 System setup

Consider a planet with mass M_p and radius R_p in an orbit with semimajor axis a_p, eccentricity e_p, and orbital angular momentum unit vector $\hat{l}_p$, around a host star of mass $M_\star$. The planet's rotation makes it oblate, giving it a mass quadrupole coefficient J_2, and has a spin orbital angular momentum unit vector $\hat{s}$. The planet's obliquity β_p is the angle between $\hat{l}_p$ and $\hat{s}$ ($\cos \beta_p = \hat{l}_p \cdot \hat{s}$).

Orbiting the planet is a massless ring system with inner (outer) truncation radius r_{in} (r_{out}), with $\hat{l} = \hat{l}(r, t)$ specifying the orbital angular momentum unit vector of a ring with semimajor axis r at time t. Two torques act on the rings. The first is the tidal torque from the distant host star:

$$T_\star = \frac{3GM_\star r^2}{4a_p^3} \left(\hat{l} \cdot \hat{l}_p \right) \left(\hat{l} \times \hat{l}_p \right), \qquad (1)$$

where we have averaged $T_\star$ over the planet's orbit, and assumed $r \ll a_p$ and the ring eccentricity $e \ll 1$. The second is the torque from the spinning oblate planet:

$$T_p = \frac{3GM_p R_p^2 J_2}{2r^3} \left(\hat{l} \cdot \hat{s} \right) \left(\hat{l} \times \hat{s} \right). \qquad (2)$$

The equilibrium surface (Laplace surface) is set by torque balance ($T_\star + T_p = 0$). Since the only stable equilibrium for $\hat{l}$ driven solely by $T_\star$ (T_p) is to be aligned with $\hat{l}_p$ ($\hat{s}$), the equilibrium value for $\hat{l}(r)$ under the combined influence of $T_\star$ and T_p must lie in the plane spanned by $\hat{l}_p$ and $\hat{s}$. Defining $\beta(r)$ as the inclination between $\hat{l}_p$ and $\hat{s}$ ($\cos \beta[r] = \hat{l}_p \cdot \hat{l}[r]$), one can solve for the equilibrium profile (e.g. Tremaine, Touma & Namouni 2009; Tamayo et al. 2013):

$$\beta(r) = \beta_p - \frac{1}{2} \arctan \left[\frac{\sin 2\beta_p}{\cos 2\beta_p + (r_L/r)^5} \right], \qquad (3)$$

where

$$r_L = \left[2 \left(1 - e_p^2 \right)^{3/2} J_2 R_p^2 a_p^3 \frac{M_p}{M_\star} \right]^{1/5}$$

$$= 0.02225 \left(1 - e_p^2 \right)^{3/10} \left(\frac{J_2}{0.1} \right)^{1/5} \left(\frac{R_p}{1 \, R_{Jup}} \right)^{2/5} \left(\frac{a_p}{5 \, au} \right)^{3/5}$$

$$\times \left(\frac{M_p}{1 \, M_{Jup}} \right)^{1/5} \left(\frac{M_\odot}{1 \, M_\star} \right)^{1/5} au \qquad (4)$$

is the Laplace radius, which denotes roughly where the torques from the distant host star and oblate planet balance (ignoring geometrical factors), and where the Laplace surface warp is strongest.

Fig. 1 displays a schematic of the Laplace surface. Interior to the Laplace radius ($r < r_L$), the torque acting on rings from the oblate planet dominates, and ring annuli are roughly aligned with the planet's equatorial plane ($\beta \approx \beta_p$). Exterior to the Laplace radius ($r > r_L$), the host star's tidal torque dominates, and ring annuli are roughly aligned with the planet's orbital plane ($\beta \approx 0$). 3D visualizations of the Laplace surface are displayed in Fig. 2, for multiple obliquity values β_p. We see the radial extent of the disc's misaligned outer region is roughly given by r_L, hence any transit signal from the circumplanetary ring system will have an effective outer radius r_L.

2.2 Test particle integrations

We perform our integrations using the WHFAST integrator (Rein & Tamayo 2015) in the open-source REBOUND N-body package (Rein & Liu 2012). We distribute 1000 test particles linearly in
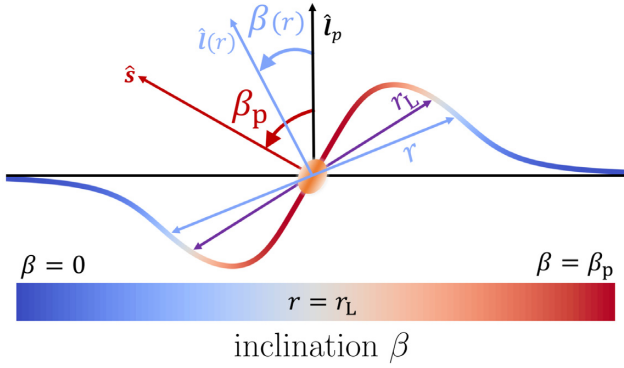
Figure 1. A schematic for our circumplanetary disc setup. The spinning oblate planet (orange) with spin orbital angular momentum unit vector $\hat{s}$ is inclined to the planet's orbital angular momentum unit vector $\hat{l}_p$ by an angle β_p (planet's obliquity). Individual satellite particles (assumed massless) orbit a distance r from the planet with orbital angular momentum unit vectors $\hat{l} = \hat{l}(r)$ on the equilibrium/Laplace surface, inclined to $\hat{l}_p$ by an angle β (test particle's obliquity; equation 3). The Laplace radius r_L (equation 4) denotes where the Laplace surface warp is (approximately) highest. We adopt the colour scheme displayed by the colour bar for β values throughout this work, unless otherwise indicated.
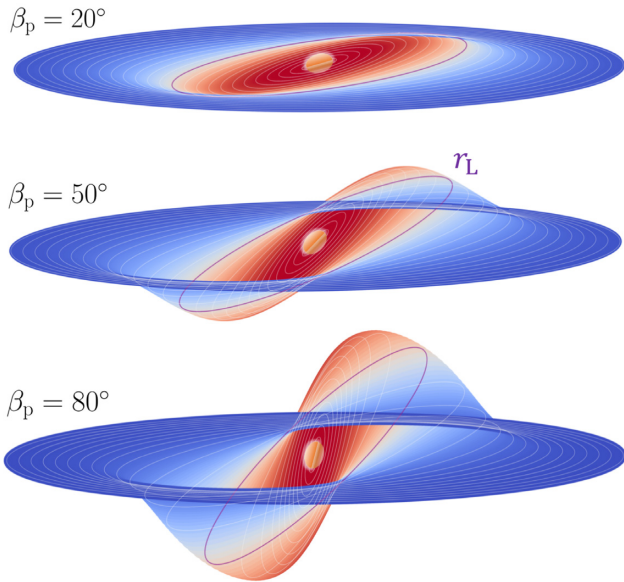

Figure 2. 3D visualizations of equilibrium/Laplace surfaces for the planetary obliquities β_p indicated. The Laplace radius r_L (equation 4) is depicted by the purple circle.

semimajor axis r from an inner truncation radius $r_{in} = 0.2\,r_L$ to an outer truncation radius $r_{out} = 2\,r_L$. We divide the 1000 particles by semimajor axis into 50 segments of 20 particles each, with segment widths $\Delta r = 0.0018\,r_L$. We integrate each segment separately, taking the segment's time-step to be 7 per cent of the inner-most particle's orbital period within the segment. With this method, we are able to integrate the outer ~800 particles for the full 16 Myr (the age of the J1407 system), but integrate the inner ~200 particles to ~3–15 Myr due to computational constraints. We note that 16 Myr corresponds to ~13–82 × 10^6 circumplanetary orbits for the outer ~800 particles, and 3–15 Myr corresponds to ~68–86 × 10^6 orbits for the inner ~200 particles. A break-down of the total integration time by particle
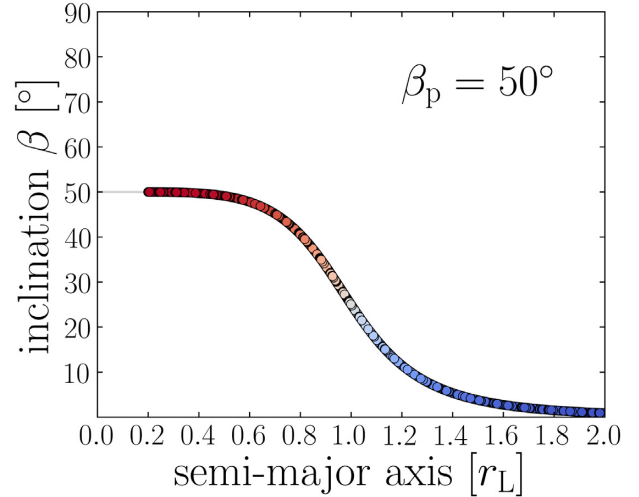

Figure 3. The inclinations β of 1000 test particles over the course of the integration (~ 3 − 16 Myr, see the text for details), initialized exactly on the Laplace surface (equation 3). The empty black circles denote test particle initial conditions, while coloured dots track the test particle's evolution. We sample the integration once every 100 yr, and randomly pick 1 in 5 of these points to display. The planet's obliquity $\beta_p = 50°$ and planet's orbital eccentricity $e_p = 0$.

and segment for one of our integrations is provided in Table A1 of Appendix A.

The host star is taken to have a mass of $M_\star = 1\,M_\odot$, and the planet's mass $M_p = 10\,M_{Jup}$, radius $R_p = 1\,R_{Jup}$, and semimajor axis $a_p = 5\,au$, with a mass quadrupole coefficient $J_2 = 0.1$. We include the force acting on the test particles from the oblate planet by adding a custom-defined additional force, using the publically available example 'J2_force' C code in the REBOUND repositories. The J_2 value chosen in our integrations is likely high, since the most oblate planet in our Solar system (Saturn) has $J_2 = 0.0162$ (Murray & Dermott 1999). We take $J_2 = 0.1$ to maximize the radial extent of the inclined region of the circumplanetary disc: since r_L has a weak dependence on J_2 ($r_L \propto J_2^{1/5}$), our results do not depend sensitively on the J_2 value. We perform a set of six simulations, varying the planet's obliquity to be $\beta_p = 20°$, $50°$, or $80°$, and its eccentricity to be $e_p = 0$ or 0.5. These values are motivated by the tentative J1407b system, but are broadly applicable to extended and inclined circumplanetary disc systems in general (see Section 4 for discussion).

A test of our simulation setup is displayed in Fig. 3. Particles are initialized with no eccentricity, and with orbital planes which lie exactly on the Laplace surface (inclinations β given by equation 3). The particle inclinations remain constant over the entire course of the simulation (~ 3 − 16 Myr), with negligible changes in the particles' longitude of ascending nodes Ω and semimajor axis r. The stability of particles on the Laplace surface confirms we have implemented the planet's J_2 and host star's tidal forces correctly, and that equation (3) describes the disc's equilibrium warp profile.

To probe the stability of a circumplanetary disc near the Laplace surface, we draw the test particle orbital parameters from distributions which differ slightly from their exact equilibrium values (Fig. 3). We draw the test particle eccentricity e from a Rayleigh distribution with mode 0.01, and argument of pericentre ω from a uniform distribution from $-\pi$ to π rad. Test particle inclinations are drawn from normal distributions centred on the equilibrium warp

profile given by equation (3), with a standard deviation of 0.01 rad. Our results are detailed in the next section.

3 RESULTS

In this section, we present the results of our N-body integrations for a collection of test particles initialized near the Laplace surface, integrating to ~ 3–16 Myr depending on the particle's orbital period (see Section 2.2 for discussion).

After running the integrations for a set of system parameters, we group particles into one of two categories: stable or unstable. If the test particle's inclination stays close to the Laplace surface ($|\Delta\beta[t]| = |\beta[t] - \beta[0]| < 0.1$ rad), and if its orbit remains close to circular ($e[t] < 0.1$), we classify the particle as stable. If the test particle becomes significantly inclined with respect to the Laplace surface ($|\Delta\beta[t]| > 0.1$ rad) or develops a significant eccentricity ($e[t] > 0.1$), we classify the particle as unstable. Misalignment with the Laplace plane can also occur if a particle's longitude of ascending node Ω moves out of the Laplace plane. Fig. B1 shows the vast majority of stable particles have Ω values close to the Laplace surface's longitude of ascending node ($\Omega = -\pi/2$).

Figs 4 and 5 plot the stable and unstable test particles' inclination β and semimajor axis r trajectories, with the change in particle eccentricity Δe, for a planet on a circular ($e_p = 0$; Fig. 4) and eccentric ($e_p = 0.5$; Fig. 5) orbit, varying the planet's obliquity β_p. For low to moderate planet obliquities ($\beta_p = 20°, 50°$), $N \gtrsim 950$ out of 1000 particles remain stable over the entire course of the integration, for circular and eccentric planetary orbits. Most particles have orbits which remain close to the Laplace surface over the disc's entire annular extent ($0.2\,r_L \lesssim r \lesssim 2.0\,r_L$). For high planet obliquities ($\beta = 80°$), only test particles close to the planet ($r \lesssim 0.71\,r_L$) or past the Laplace radius ($r \gtrsim 1.05\,r_L$) remain stable over the course of the integration.

We expect every instability/resonance observed in our integrations to be secular over the test particle's orbit. Comparing the particle's mean-motion $n = \sqrt{GM_p/r^3}$ to the planet's $n_p = \sqrt{GM_\star/a_p^3}$, we see

$$\frac{n}{n_p} = \frac{89}{(1-e_p^2)^{9/20}} \left(\frac{0.1}{J_2}\right)^{1/5} \left(\frac{M_p}{M_{Jup}}\right)^{1/5} \left(\frac{1\,M_\odot}{M_\star}\right)^{1/5}$$
$$\times \left(\frac{a_p}{5\,au}\right)^{3/5} \left(\frac{1\,R_{Jup}}{R_p}\right)^{3/5} \left(\frac{r_L}{r}\right)^{3/2}. \quad (5)$$

Since $n \gg n_p$ when $r \lesssim$ few r_L, we expect mean-motion resonances to be unimportant. As expected, all stable particles in our integrations have negligible changes in their initial r values, with semimajor axis variations $|r(t) - r(0)| \lesssim 0.01\,r(0)$. Unstable particles may have significant changes in their r values when the particle becomes unbound to or crashes into the planet, or from numerical effects when e approaches unity.

Two main instabilities are observed in our integrations. The most extended instability in r is a Lidov–Kozai (LK) instability which occurs for the $\beta_p = 80°$ integration when particles orbit near the Laplace radius ($0.71\,r_L \lesssim r \lesssim 1.05\,r_L$), originally predicted to occur by Tremaine et al. (2009) when $\beta_p > 68.875°$. The second instability occurs in the disc's inner regions ($r \lesssim 0.3 - 0.5\,r_L$), regardless of the planet's β_p value. The instabilities occur regardless of the planetary orbit's eccentricity value (Figs 4 and 5). To confirm these instabilities are robust to the integration time-step, we re-performed our integrations with a time-step set at 1 per cent the innermost particle's period in each disc segment for 10^4 yr, and observed the

instabilities were qualitatively the same. We discuss both instabilities in greater detail in Sections 3.1 and 3.2.

For the planet on an eccentric orbit ($e_p = 0.5$, Fig. 5) with an obliquity $\beta_p = 50°$, we note an additional instability not present in the similar integration for a planet on a circular orbit (Fig. 4), which occurs on two narrow regions around $r \approx 0.86\,r_L$ and $r \approx 0.98\,r_L$. These instabilities excite test particle inclinations and eccentricities ($\Delta\beta > 0.1$ rad and $e > 0.1$), but to relatively modest values ($\Delta\beta \lesssim 0.2$ rad and $e \lesssim 0.2$). This instability may be due to octopole-level perturbations from the distant host star (e.g. Katz, Dong & Malhotra 2011; Naoz et al. 2011; Li et al. 2014), but we do not discuss this instability any further in this work.

In our integrations with a planet on an eccentric orbit, the projection of the planet's spin axis $\hat{s}$ on to the planet's orbital plane lies perpendicular to the planet's pericentre direction. Our integrations with $\hat{s}$ pointing in the same or opposite direction as the planet's pericentre, which we do not show, find similar results.

3.1 Lidov–Kozai instability

This subsection analyses the LK instability seen in our high planetary obliquity ($\beta_p = 80°$) integrations in greater detail. Fig. 6 plots the inclination β and eccentricity e evolution of three representative test particles which become LK unstable during the $\beta_p = 80°$ integration for a planet on a circular orbit (bottom-right-hand panel of Fig. 4). We see over secular time-scales (few 10^3 yr), the test particle β value decreases when the e value becomes sufficiently large, characteristic of LK oscillations (Kozai 1962; Lidov 1962). Many particles are eventually ejected from the system or crash into the planet, hence the scattering and pile-up at $r \approx 0$ in the bottom right-hand panels of Figs 4 and 5. Our plots do not display β variations for particles with $r \gtrsim 0.9\,r_L$, because the particles become unbound ($e > 1$) before the change in β can be sampled.

Previous work done by Tremaine et al. (2009) predicted test particles near the Laplace surface would be susceptible to the LK instability when $\beta_p > 68.875°$, since the host star's tidal torque may overcome the stabilizing influence of the oblate planet's torque, and cause the particle's eccentricity to grow exponentially (see also Martin et al. 2014; Tremaine & Yavetz 2014; Lubow & Ogilvie 2017; Zanazzi & Lai 2017b). Tremaine et al. (2009) found the particles which could become LK unstable had r values from about $0.95\,r_L$ to $1.1\,r_L$ when $\beta_p = 80°$ and $e_p = 0$ (roughly estimated from their Fig. 2). We find the annular extent of the disc susceptible to the LK instability to be more extended ($0.71\,r_L \lesssim r \lesssim 1.05\,r_L$). Further work is needed to understand why our integrations find LK unstable particles when $r \lesssim 0.95\,r_L$.

3.2 Ivection instability

In all of our integrations, test particles close to the host star ($r \lesssim 0.3$–$0.5\,r_L$) occasionally have large excitations in their inclinations β. This subsection argues the β excitation when $r \lesssim 0.3$–$0.5\,r_L$ is due to an ivection resonance (Xu & Fabrycky 2019), and examines the orbital evolution for particles which undergo ivection resonance.

The ivection resonance is very similar to the more well-studied evection resonance (e.g. Touma & Wisdom 1998; Ćuk & Burns 2004; Yokoyama et al. 2008; Frouard, Fouchard & Vienne 2010; Spalding, Batygin & Adams 2016; Xu & Lai 2016). In the context of satellites orbiting giant planets, the evection resonance occurs when the apsidal precession rate $\dot\omega$, driven by either the planet's mass quadrupole or host star's tidal torque, matches the mean-motion of the planet $n_p =$
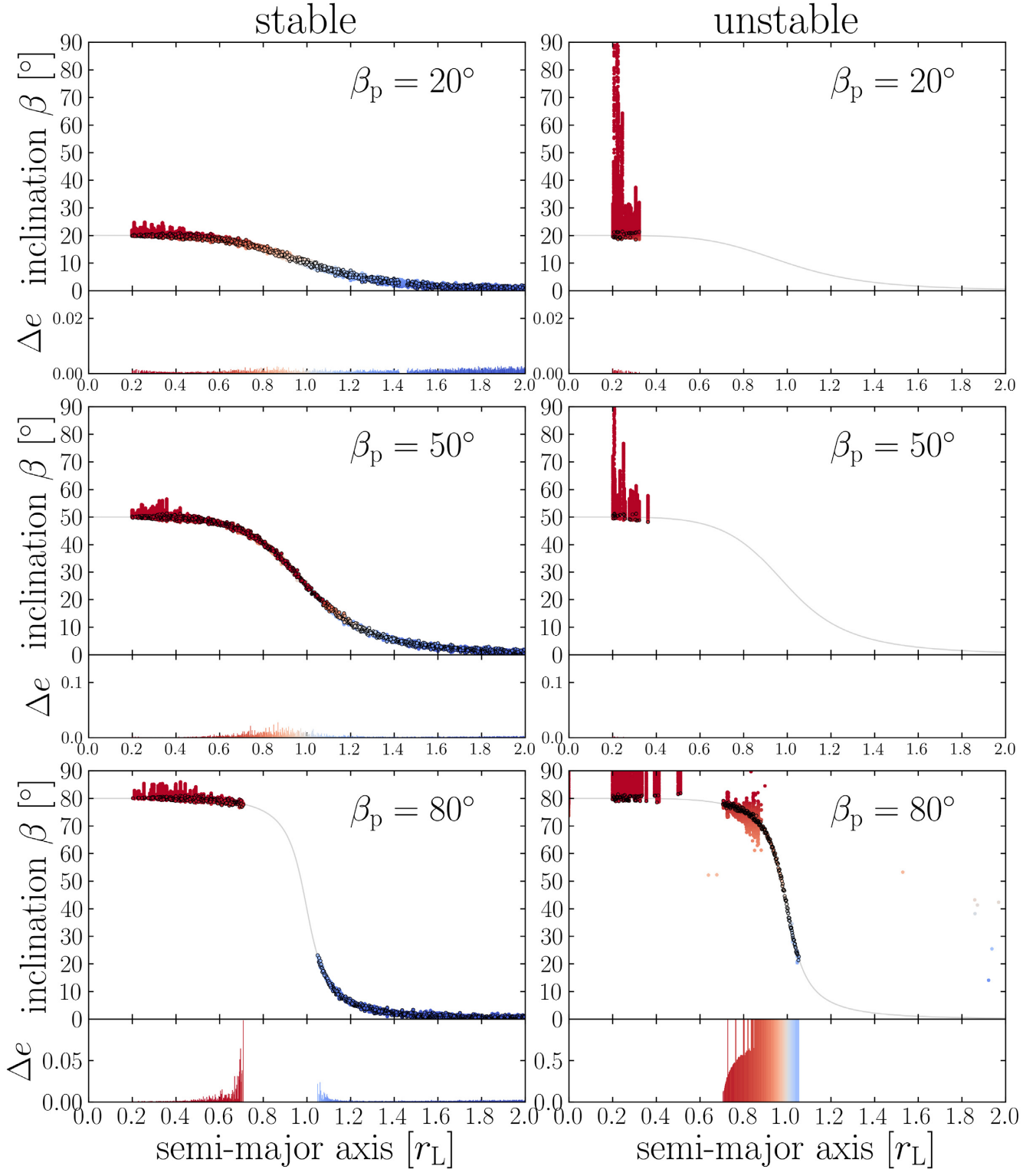
Figure 4. *N*-body integrations of test particles initialized near the Laplace surface (see Section 2.2 for details), for a planet on a circular orbit ($e_p = 0$), for the planetary obliquities β_p as indicated. The top plot in each panel shows inclinations β of $N = 1000$ particles over the full course of each integration, with empty black circles indicating their initial positions around the Laplace surface (grey line) and coloured points tracking their evolution. The bottom plot in each panel shows the change in particle eccentricity $\Delta e = \max[e(t)]$ over the course of the integration. Particles with orbits that remain near the Laplace surface ($|\Delta\beta| = |\beta[t] - \beta[0]| < 0.1$ rad and $e[t] < 0.1$) are categorized as stable (left-hand panel), and particles that become significantly inclined to the Laplace surface ($|\Delta\beta| > 0.1$ rad) or develop significant eccentricities ($e > 0.1$) as unstable (right-hand panel). Each integration is sampled once every 100 yr ($\sim$11 planet orbits), and we randomly select 1 in 5 points in each sample to plot. Here, $r_L = 0.035$ au $= 0.048\,r_H$, where $r_H = a_p(1 - e_p)[M_p/(3M_\star)]^{1/3}$ is the Hill radius.
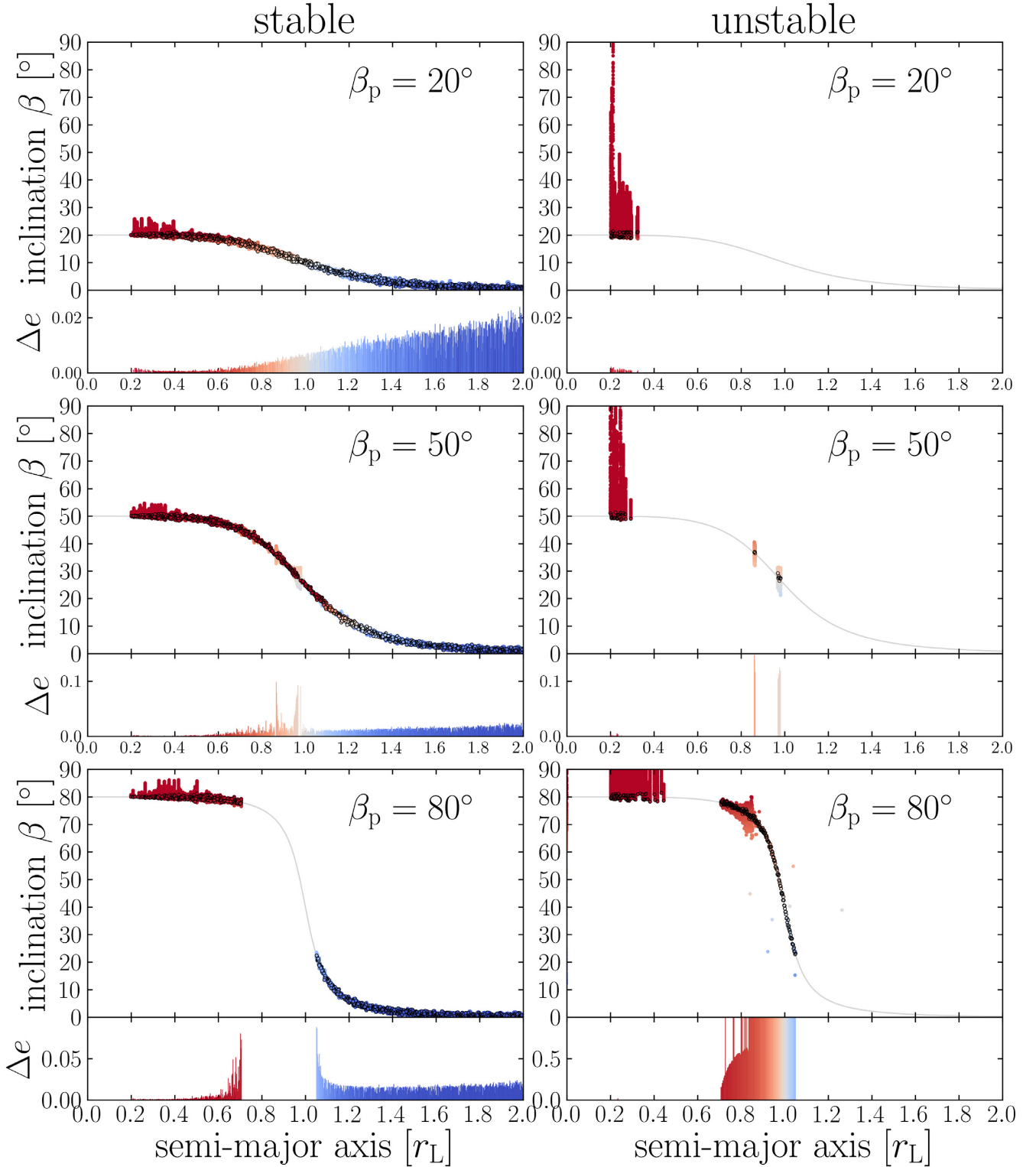
Figure 5. Same as Fig. 4, except the planet lies on an eccentric orbit ($e_p = 0.5$). Here, $r_L = 0.032$ au $= 0.088\, r_H$, where $r_H = a_p(1 - e_p)[M_p/(3M_\star)]^{1/3}$ is the Hill radius.

$\sqrt{GM_\star/a_p^3}$. The effect of this secular-orbital resonance (averaged over the satellites orbit, but not the planet's) is to cause a significant excitation in the satellite's eccentricity e, with little corresponding excitation in the satellite's inclination β. Ivection resonance is an

analogous secular-orbital resonance, but occurs when the precession rate of the satellite's longitude of ascending node $\dot{\Omega}$ matches n_p, and mainly excites the satellite's β rather than e. Although the system setup for the recently discovered ivection resonance (Xu & Fabrycky 2019) is different from this work, consisting of two nearly coplanar
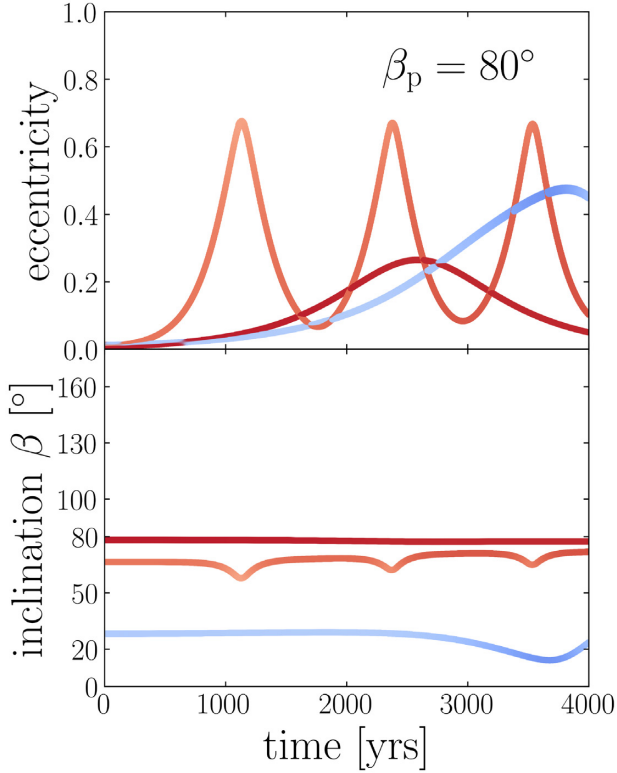
Figure 6. Evolution of test particle orbital eccentricity e (top panel) and inclination β (bottom panel) for a few representative test particles undergoing the Lidov-Kozai instability, with semimajor axis $a = 0.720\,r_{\rm L}$ (dark red), $a = 0.907\,r_{\rm L}$ (light red), and $a = 1.028\,r_{\rm L}$ (blue, see Fig. 1 for colour scheme). We select particles from the $e_{\rm p} = 0$, $\beta_{\rm p} = 80°$ integration (Fig. 4, bottom right-hand panel). We display the test particle evolution for the first 4000 yr, sampled twice per year.

planets with a binary companion perturber, there is no reason to expect ivection resonance does not occur for satellites orbiting giant planets.

Within a factor of a few, evection and ivection should occur at similar r values, since the apsidal $\dot\omega$ and nodal $\dot\Omega$ precession rates driven by the planet's mass quadrupole are similar. Ignoring geometrical factors, the apsidal/nodal precession rate on the test particle from the oblate planet is (i.e. Tremaine et al. 2009; Tremaine & Yavetz 2014)

$$\dot\omega|_{\rm s} \sim \dot\Omega|_{\rm s} \sim \frac{J_2 R_{\rm p}^2 (GM_{\rm p})^{1/2}}{r^{7/2}}. \qquad (6)$$

Evection resonance occurs when $\dot\omega|_{\rm s} \sim n_{\rm p}$, while ivection resonance occurs when $\dot\Omega|_{\rm s} \sim n_{\rm p}$. Solving for the resonant semimajor axis $r_{\rm res}$ where $\dot\omega|_{\rm s} \sim \dot\Omega|_{\rm s} \sim n_{\rm p}$, we find

$$
\begin{aligned}
r_{\rm res} &\sim J_2^{2/7} R_{\rm p}^{4/7} a_{\rm p}^{3/7} (M_{\rm p}/M_\star)^{1/7}\\
&= \frac{0.22}{(1 - e_{\rm p}^2)^{3/10}} \left(\frac{J_2}{0.1}\right)^{3/35} \left(\frac{R_{\rm p}}{1\,{\rm R_{Jup}}}\right)^{6/35} \left(\frac{5\,{\rm au}}{a_{\rm p}}\right)^{6/35}\\
&\quad \times \left(\frac{M_\star}{1\,{\rm M_\odot}}\right)^{2/35} \left(\frac{1\,{\rm M_{Jup}}}{M_{\rm p}}\right)^{2/35} r_{\rm L}.
\end{aligned} \qquad (7)
$$

From estimate (7), we see evection and ivection may be important near the disc's inner truncation radius $r_{\rm in} = 0.2\,r_{\rm L}$.

Fig. 7 plots the evolution of test particle e and β values which undergo ivection resonance. We see β undergoes oscillations, while e remains relatively constant, as expected from ivection (Xu & Fabrycky 2019). Although oscillations in β are a few tens of
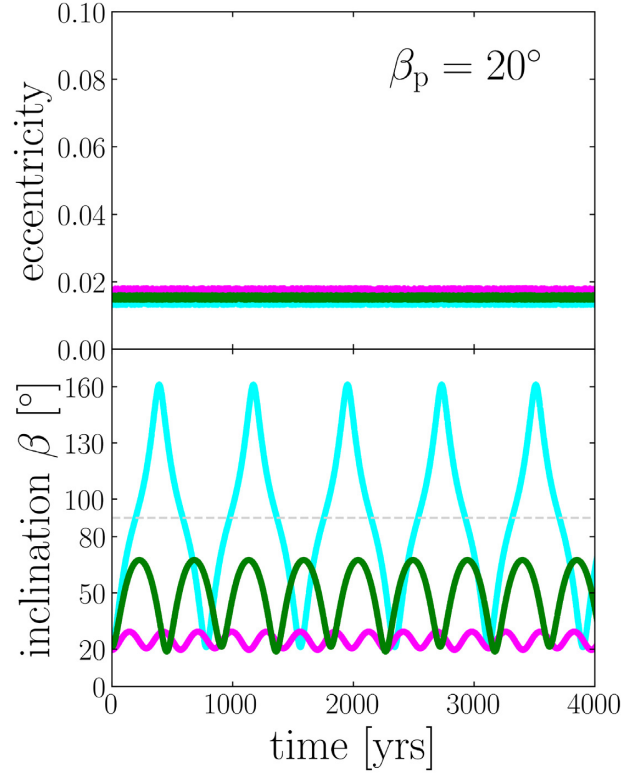

Figure 7. Evolution of test particle eccentricities e (top panel) and inclinations β (bottom panel) undergoing the ivection instability, from the $\beta_{\rm p} = 20°$, $e_{\rm p} = 0$ integration (top right-hand panel of Fig. 4). Different coloured lines denote the orbital evolution of three separate particles, with initial orbital elements $(a, e, \beta, \omega) = (0.200\,r_{\rm L}, 0.015, 21.0°, 70.8°)$ (cyan), $(a, e, \beta, \omega) = (0.209\,r_{\rm L}, 0.017, 19.5°, -29.1°)$ (magenta), and $(a, e, \beta, \omega) = (0.232\,r_{\rm L}, 0.016, 21.3°, -40.7°)$ (green), with Ω always initialized to $\Omega = -90°$. The dashed grey line at $90°$ shows the threshold for prograde ($\beta < 90°$) versus retrograde ($\beta > 90°$) orbits. We display integrations run for 4000 yr, sampled twice per year.

degrees for most test particles, some particles display much larger oscillations, ocassionally even becoming retrograde ($\beta > 90°$ see Fig. B2). Additional visualizations of the variation in particle β-excitation amongst the ivection-unstable particles are provided in Fig. B3. We also ran integrations after decreasing the disc's $r_{\rm in}$ (not shown), and found the disc experienced evection resonance (e excited, β relatively constant) at $r \approx 0.1\,r_{\rm L}$. Our exploration of ivection and evection is preliminary, and a more detailed investigation is outside the scope of this work.

4 DISCUSSION

In this section, we discuss the implications of our work for the J1407b system, as well as future work and theoretical uncertainties.

4.1 Implications for the J1407b system

4.1.1 Are exomoons present?

The light-curve of J1407 is highly variable and structured, argued to be caused by gaps in J1407b's circumplanetary disc, visible during the system's transit. Exomoons orbiting J1407b have been invoked to carve these gaps, since this structure should otherwise be erased by internal disc interactions on dynamical time-

scales (Van Werkhoven et al. 2014; Kenworthy & Mamajek 2015). In our Solar system, stable and long-lived gaps are created by resonant satellite–disc interactions, and similar processes may be happening in the J1407 system. Kenworthy & Mamajek (2015) even estimated the maximum mass of a moon that could have cleared the largest gap in their ring model (0.0267 au wide at 0.4 au), which they found to be 8 Earth masses. However, Sutton (2019) tried to reproduce this same gap in *N*-body simulations by placing moons orbiting exterior to the circumplanetary disc, at the locations of mean motion resonances with the gap, and concluded this scenario carved a gap which was too narrow to explain the observations.

If the disc is not flat, but warped by the competing influence of the tidal torque from the host star and the torque from the spinning planet, we find that secular instabilities can potentially carve gaps in collisionless discs. Ivection resonance could produce highly structured gaps in the inner regions of the disc, and at sufficiently high planetary obliquities ($\beta_p > 68.875°$), the secular instability of Tremaine et al. (2009) could result in such a large gap near the system's Laplace radius r_L (equation 4) that there appears to be distinct inner and outer circumplanetary discs. Neither instability which may carve gaps in the disc requires the presence of exomoons.

4.1.2 Is the disc warped?

A number of challenges remain regarding the stability of the putative disc orbiting J1407b. In order to achieve the high transverse velocities implied by the rapid changes in the J1407 light curve, either the companion J1407b must be on a tight orbit ($a_p < 6$ au), or we are observing the periastron passage of the companion on a very eccentric orbit ($e_p > 0.7$; Kenworthy et al. 2014; Mentel et al. 2018). Whether J1407b lies on an eccentric orbit which transits at periastron, or on a tight circular orbit, the J1407b disc would fill a significant fraction (70–100 per cent) of the companion's Hill sphere (Mentel et al. 2018). A disc orbiting retrograde was found by Rieder & Kenworthy (2016) to survive longer (∼110 000 yr) around a substellar-mass (60–100 M_{Jup}) companion on an 11 yr orbit than a disc orbiting prograde, but this poses the additional challenge of explaining the formation of a retrograde circumplanetary disc.

Furthermore, while the flat, inclined, and extended best-fitting ring model of Kenworthy & Mamajek (2015) reproduces many of the features in the observed J1407 light curve, it does not reproduce them all. The authors suggest that better fits to the data may be achieved by a model that allows for additional degrees of freedom for the rings, such as warping or precession. A disc around J1407b that warps to the Laplace surface, such as we investigate in this work, may produce better fits to the data. It may also be a solution to the challenges in stability faced by its flat counterpart.

The remaining question is then the maximum size of the circum-secondary disc around J1407b. We review the order-of-magnitude estimates of Mamajek et al. (2012) constraining the size of J1407b's disc, but note similar estimates can be used to constrain properties of other tentative circumsecondary discs. The time over which J1407 is eclipsed is $t_{ecl} \sim 54$ d (Mamajek et al. 2012). For this eclipse time to be due to a circumsecondary disc, we must have

$$t_{ecl} \sim \frac{2r_{out}}{v_{orb}} = \frac{2r_{out}}{n_p a_p F(e_p, f_{ecl})}, \tag{8}$$

where v_{orb} and f_{ecl} are the orbital velocity and true anomaly of the companion during eclipse, e_p, $n_p = \sqrt{GM_\star/a_p^3}$, and a_p are the

companion's eccentricity, mean-motion, and semimajor axis, while r_{out} is the outer radius of the disc. Here,

$$F(e_p, f_{ecl}) = \sqrt{\frac{1 + 2e_p \cos f_{ecl} + e_p^2}{1 - e_p^2}} \tag{9}$$

is how much v_{orb} can be increased/decreased from a non-zero e_p. Observations constrain the companion's orbital period P_{orb} and eclipse duration t_{ecl}, so we solve for r_{out}:

$$r_{out} \sim F(e_p, f_{ecl}) \left(\frac{\pi G M_\star}{4 P_{orb}}\right)^{1/3} t_{ecl}$$
$$= 0.080 \, F(e_p, f_{ecl}) \left(\frac{M_\star}{0.9 \, M_\odot}\right)^{1/3} \left(\frac{30 \, \text{yrs}}{P_{orb}}\right)^{1/3} \left(\frac{t_{ecl}}{30 \, \text{days}}\right) \, \text{au}. \tag{10}$$

For a warped disc to be a feasible model, the tilted disc region's size must be large enough to produce the ∼54 d transit seen by Mamajek et al. (2012). Since the inclined disc's size r_{inc} is $r_{inc} \sim r_L$ (see Fig. 2, see also Schlichting & Chang 2011), we require $r_{out} \sim r_L$ for a disc warped along the secondary's Laplace surface to explain the observations. Fig. 8 calculates the Laplace radius r_L (equation 4) of a warped disc surrounding a companion to J1407 as a function of the companion's mass M_p for two a_p values, and compares r_L to the observationally constrained outer disc radius r_{out}. We find that a warped circumplanetary disc ($M_p \lesssim 13 \, M_{Jup}$) around J1407b cannot extend to large enough radii to explain the observations. An eccentric companion orbit creates a larger discrepancy between r_L and r_{out}. A substellar companion on a large, circular orbit could produce a long enough transit signal, though it would be inconsistent with the transverse velocities required to produce the rapid changes observed in J1407's light curve. For a warped disc to explain J1407b's transit, additional forces must work to increase the radius of r_{inc} to be greater than r_L, which we discuss in the next subsection.

4.2 Theoretical uncertainties and future work

This work studies the dynamics of collisionless circumplanetary debris discs, neglecting internal processes that may modify the orbits of massless particles from which the disc is composed. Radiation pressure is widely known to have a significant impact on circumstellar debris discs (e.g. Lee & Chiang 2016), and can modify the Laplace surface for circumplanetary discs (Tamayo et al. 2013). Additional forces within the disc – such as disc self-gravity (Ward 1981; Zanazzi & Lai 2017a), along with bending waves (i.e. Zanazzi & Lai 2018) and viscous torques (Tremaine & Davis 2014) in hydrodynamical discs – can modify the equilibrium warp profile. These additional external or internal forces/torques can potentially increase the radius of the disc's tilted region r_{inc} to be greater than r_L (equation 4). In particular, Zanazzi & Lai (2017a) found disc self-gravity can increase r_{inc} to become comparable to the observationally constrained r_{out} for J1407b's disc (see Section 4.1.2 for discussion), but the disc mass required to do so ($M_{disk} \gtrsim$ few $10^{-3} \, M_p$) may cause the disc to become gravitationally unstable. Moreover, since this disc is optically thick (Kenworthy & Mamajek 2015), particle collisions are likely relevant (e.g. Wisdom & Tremaine 1988; Rein & Papaloizou 2010; Latter, Ogilvie & Chupeau 2012). We leave investigations of these effects to future works.

We argue that ivection resonance (Xu & Fabrycky 2019) causes the inclination excitation observed in the inner region of the circumplanetary disc in our integrations (see Section 3.2 for discussion), but further theoretical work is needed to understand its role in detail. We believe it was not investigated before because previous studies
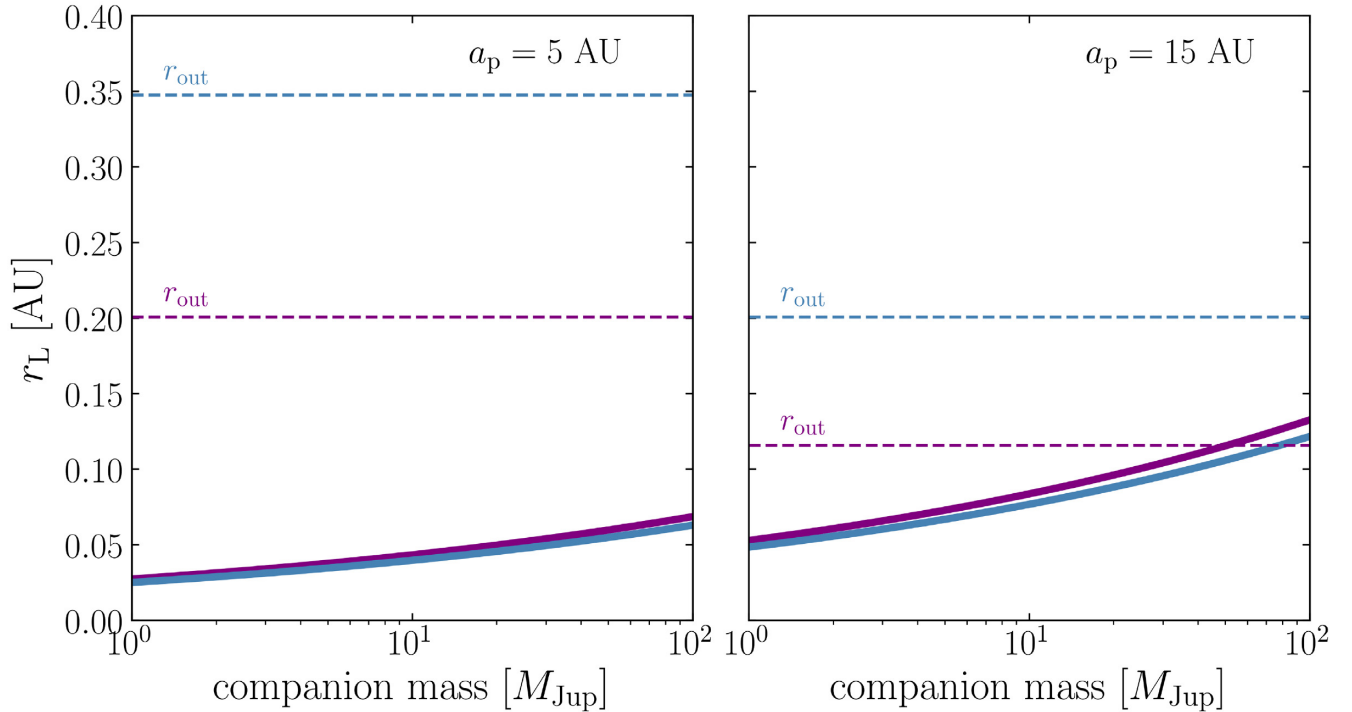
Figure 8. The Laplace radius (equation 4; solid lines) as a function of companion mass M_p, compared with the observationally constrained radius of J1407b's disc r_{out} (equation 10; dashed lines), for circular ($e_p = 0$; blue lines) and eccentric ($e_p = 0.5$; purple lines) companion orbits. For a transit signal to be produced by J1407b's disc, we require $r_L \sim r_{out}$ (see also Fig. 2). Here, $M_\star = 0.9\,M_\odot$, $R_p = 1\,R_{Jup}$, $t_{ecl} = 54\,d$, $f_{ecl} = 0$, and $J_2 = 0.5$.

on satellites around massive planets had the satellite semimajor axis r slowly increase due to tidal dissipation (e.g. Touma & Wisdom 1998; Ćuk & Burns 2004). In our preliminary integrations reducing the disc's inner truncation radius r_{in} (which we do not show), we find the location of evection resonance ($r \lesssim 0.1\,r_L$) to be interior to ivection resonance ($r \approx 0.2 - 0.5\,r_L$). Ivection resonance may be particularly important for exomoons, since the resonant semimajor axis r_{res} (equation 7) will increase as the planet migrates inward through its natal protoplanetary disc (Spalding et al. 2016).

To date, all studies examining the transit signatures of circumplanetary disc systems assume a flat disc, or coplanar rings, misaligned with the planet's orbital plane. For the tentative detections of extended circumplanetary discs (e.g. Mamajek et al. 2012; Osborn et al. 2017; Rappaport et al. 2019; Saito et al. 2019), our study shows such discs are likely to be significantly warped. Studies of transit signatures from warped circumplanetary discs would be of interest for these extended systems.

5 CONCLUSIONS

Motivated by the tentative detection of extended circumplanetary/circumsecondary disc/ring systems, we explore the dynamical stability of particles orbiting near the equilibrium surface (Laplace surface) set by the balance between the tidal torque from the host star with the torque from the spinning planet's mass quadrupole, using *N*-body integrations. By integrating test particle orbits drawn from distributions close to the Laplace surface, we simulate the evolution of a collisionless circumplanetary debris disc system. We perform our simulations for three planetary obliquities ($\beta_p = 20°$, $50°$, $80°$) and two values of eccentricity ($e_p = 0$, 0.5). Our main findings are as follows:

(i) For all planet obliquities ($\beta_p = 20°$, $50°$, $80°$) and eccentricities ($e_p = 0$, 0.5), much of the warped circumplanetary disc remains stable over the course of our integrations ($\sim 3 - 16\,Myr$; Section 3).

(ii) Two dynamical resonances/instabilities can potentially carve gaps in the circumplanetary disc: the Lidov–Kozai mechanism (Section 3.1) and ivection resonance (Section 3.2). Such gaps could be detectable if the circumplanetary disc system transits its host star, and would not necessarily imply the existence of exomoons (Section 4.1.1).

We also investigate if a disc orbiting the hypothesized J1407 companion could be misaligned by J1407b's mass quadrupole, and extend to large enough radii to match the observed eclipse duration seen in Mamajek et al. (2012). We find the disc may become misaligned at sufficiently large distances from J1407b only for a substellar-mass ($M_p \gtrsim 50\,M_{Jup}$) companion on a large ($a \gtrsim 15\,au$) nearly circular orbit. Additional forces are needed to extend the misaligned region of the disc around J1407b to explain J1407's eclipse duration.

Shortly after this work was published, Kenworthy et al. (2020) used the Atacama Large Millimetre/submillimetre Array (ALMA) to detect potential submillimetre continuum emission around the star J1407, and attempted to detect thermal emission from the J1407b exoring system. Kenworthy et al. (2020) detected optically thin dust emission orbiting a substellar object, consistent with a ring system if J1407b lies on an unbound orbit. If this detected substellar object is indeed the J1407b ring system, our stability constraints must be modified to account for an impulsive encounter between the disc and host star. Our results remain applicable to the general stability of extended circumsecondary discs.

Photometric techniques may soon bring direct observations of circumplanetary discs to reality, providing opportunity to put to the

test the regions of instability we predict in this work. Discussions of circumplanetary (or circumsecondary) debris discs, exorings, or even exomoons should consider the geometry of the Laplace surface.

SOFTWARE

`astropy` (Robitaille et al. 2013; Price-Whelan et al. 2018), `jupyter notebook` (Kluyver et al. 2016), `matplotlib` (Hunter 2007), `numPy` (Walt, Colbert & Varoquaux 2011), `pandas` (McKinney 2010), `rebound` (Rein & Liu 2012), `sciPy` (Virtanen et al. 2020).

DATA AVAILABILITY

The data underlying this article will be shared on reasonable request to the corresponding author.

REFERENCES

Aizawa M., Uehara S., Masuda K., Kawahara H., Suto Y., 2017, AJ, 153, 193
Ansdell M. et al., 2016, ApJ, 816, 69
Ansdell M. et al., 2019, MNRAS, 483, 3579
Barnes J. W., Fortney J. J., 2004, ApJ, 616, 1193
Brown T. M., Charbonneau D., Gilliland R. L., Noyes R. W., Burrows A., 2001, ApJ, 552, 699
Christiaens V., Cantalloube F., Casassus S., Price D. J., Absil O., Pinte C., Girard J., Montesinos M., 2019, ApJ, 877, L33
Cody A. M. et al., 2014, AJ, 147, 82
Ćuk M., Burns J. A., 2004, AJ, 128, 2518
Frouard J., Fouchard M., Vienne A., 2010, A&A, 515, A54
Hedges C., Hodgkin S., Kennedy G., 2018, MNRAS, 476, 2968
Heising M. Z., Marcy G. W., Schlichting H. E., 2015, ApJ, 814, 81
Hunter J. D., 2007, Comput. Sci. Eng., 9, 90
Katz B., Dong S., Malhotra R., 2011, Phys. Rev. Lett., 107, 181101
Kenworthy M. et al., 2014, MNRAS, 446, 411
Kenworthy M. A., Mamajek E. E., 2015, ApJ, 800, 126
Kenworthy M. A. et al., 2020, A&A, 633, A115
Kluyver T. et al., 2016, in Loizides F., Schmidt B., eds, Positioning and Power in Academic Publishing: Players, Agents and Agendas, ELPUB, p. 87
Kozai Y., 1962, AJ, 67, 591

Laplace P.-S., Celeste M., 1805, Courcier, Paris
Latter H. N., Ogilvie G. I., Chupeau M., 2012, MNRAS, 427, 2336
Lee E. J., Chiang E., 2016, ApJ, 827, 125
Li G., Naoz S., Kocsis B., Loeb A., 2014, ApJ, 785, 116
Lidov M. L., 1962, Planet. Space Sci., 9, 719
Lubow S. H., Ogilvie G. I., 2017, MNRAS, 469, 4292
Mamajek E. E., Quillen A. C., Pecaut M. J., Moolekamp F., Scott E. L., Kenworthy M. A., Cameron A. C., Parley N. R., 2012, AJ, 143, 72
Martin R. G., Nixon C., Lubow S. H., Armitage P. J., Price D. J., Doğan S., King A., 2014, ApJ, 792, L33
McGinnis P. T. et al., 2015, A&A, 577, A11
McKinney, 2010, in van der Walt S., Millman J., ed., Proceedings of the 9th Python in Science Conference, p. 51
Mentel R. et al., 2018, A&A, 619, A157
Murray C. D., Dermott S. F., 1999, Solar System Dynamics. Cambridge Univ. Press, Cambridge
Naoz S., Farr W. M., Lithwick Y., Rasio F. A., Teyssandier J., 2011, Nature, 473, 187
Ohta Y., Taruya A., Suto Y., 2009, ApJ, 690, 1
Osborn H. P. et al., 2017, MNRAS, 471, 740
Osborn H. P. et al., 2019, MNRAS, 485, 1614
Pecaut M. J., Mamajek E. E., 2013, ApJS, 208, 9
Price-Whelan A. et al., 2018, AJ, 156, 123
Rappaport S. et al., 2018, MNRAS, 474, 1453
Rappaport S. et al., 2019, MNRAS, 485, 2681
Rein E., Ofir A., 2019, MNRAS, 490, 1111
Rein H., Liu S.-F., 2012, A&A, 537, A128
Rein H., Papaloizou J. C. B., 2010, A&A, 524, A22
Rein H., Tamayo D., 2015, MNRAS, 452, 376
Rieder S., Kenworthy M. A., 2016, A&A, 596, A9
Robitaille T. P. et al., 2013, A&A, 558, A33
Rodriguez J. E. et al., 2018, ApJ, 859, 150
Saito R. K. et al., 2019, MNRAS, 482, 5000
Sandford E., Kipping D., 2019, AJ, 157, 42
Santos N. C. et al., 2015, A&A, 583, A50
Schlichting H. E., Chang P., 2011, ApJ, 734, 117
Schneider J., 1999, Acad. Sci. Paris C. R. B, 6, 621
Spalding C., Batygin K., Adams F. C., 2016, ApJ, 817, 18
Sucerquia M., Alvarado-Montes J., Ramírez V., Zuluaga J. I., 2017, MNRAS, 472, L120
Sutton P. J., 2019, MNRAS, 486, 1681
Szulágyi J., Garufi A., 2019, preprint (arXiv:1906.01416)
Szulágyi J., Plas G. v. d., Meyer M. R., Pohl A., Quanz S. P., Mayer L., Daemgen S., Tamburello V., 2018, MNRAS, 473, 3573
Szulágyi J., Dullemond C. P., Pohl A., Quanz S. P., 2019, MNRAS, 487, 1248
Tamayo D., Burns J. A., Hamilton D. P., Nicholson P. D., 2013, AJ, 145, 54
Touma J., Wisdom J., 1998, AJ, 115, 1653
Tremaine S., Davis S. W., 2014, MNRAS, 441, 1408
Tremaine S., Yavetz T. D., 2014, Am. J. Phys., 82, 769
Tremaine S., Touma J., Namouni F., 2009, AJ, 137, 3706
Van Werkhoven T., Kenworthy M., Mamajek E., 2014, MNRAS, 441, 2845
Virtanen P. et al., 2020, Nat. Methods, 17, 261
Walt S. v. d., Colbert S. C., Varoquaux G., 2011, Comput. Sci. Eng., 13, 22
Ward W. R., 1981, Icarus, 46, 97
Wisdom J., Tremaine S., 1988, AJ, 95, 925
Xu W., Fabrycky D., 2019, preprint (arXiv:1904.02290)
Xu W., Lai D., 2016, MNRAS, 459, 2925
Yokoyama T., Vieira Neto E., Winter O. C., Sanchez D. M., Brasil P. I. d. O., 2008, Math. Probl. Eng., 2008
Zanazzi J. J., Lai D., 2017a, MNRAS, 464, 3945
Zanazzi J. J., Lai D., 2017b, MNRAS, 467, 1957
Zanazzi J. J., Lai D., 2018, MNRAS, 477, 5207
Zuluaga J. I., Kipping D. M., Sucerquia M., Alvarado J. A., 2015, ApJ, 803, L14

APPENDIX A: TOTAL INTEGRATION TIME BREAK-DOWN

As mentioned in Section 2, our integration times for test particles within each disc segment (semimajor axis bin) are set by computa-tional constraints. Table A1 lists the break-down of integration times by particle segment, for the $e_p = 0$, $\beta_p = 50°$ integration; the other integrations displayed in Figs 4 and 5 are similar.

Table A1. Total integration time by disc segment for the $e_p = 0$, $\beta_p = 50°$ integration. Columns are: test particle index (#), the segment of the disc it belongs to (seg.), its semimajor axis (a, in units of r_L), the total integration time of that segment (T_{tot} 10^6 [yr]), and how many circumplanetary test particle orbits to which T_{tot} equates to (10^6 [orbits]). All particles in Segment 1 are shown; only the first is shown for segments 2–49; first and last are shown for Segment 50. Segments that are *not* integrated to 16 Myr are indicated by ∗.

		Segments 1, 2–16					Segments 17–50		
#	seg.	a [r_L]	T_{tot} 10^6 (yr)	10^6 (orbits)	#	seg.	a [r_L]	T_{tot} 10^6 (yr)	10^6 (orbits)
0	1 ∗	0.2001	3.2646	85.669	320	17	0.7761	16.0000	54.971
1		0.2016	3.2646	84.737	340	18	0.8121	16.0000	51.356
2		0.2038	3.2646	83.370	360	19	0.8480	16.0000	48.123
3		0.2055	3.2646	82.327	380	20	0.8840	16.0000	45.215
4		0.2071	3.2646	81.368	400	21	0.9199	16.0000	42.593
5		0.2090	3.2646	80.239	420	22	0.9560	16.0000	40.204
6		0.2107	3.2646	79.274	440	23	0.9920	16.0000	38.039
7		0.2125	3.2646	78.278	460	24	1.0280	16.0000	36.056
8		0.2142	3.2646	77.373	480	25	1.0640	16.0000	34.243
9		0.2163	3.2646	76.199	500	26	1.0999	16.0000	32.578
10		0.2180	3.2646	75.356	520	27	1.1360	16.0000	31.040
11		0.2197	3.2646	74.461	540	28	1.1719	16.0000	29.622
12		0.2218	3.2646	73.421	560	29	1.2080	16.0000	28.305
13		0.2234	3.2646	72.630	580	30	1.2441	16.0000	27.083
14		0.2254	3.2646	71.670	600	31	1.2803	16.0000	25.942
15		0.2268	3.2646	70.988	620	32	1.3161	16.0000	24.892
16		0.2287	3.2646	70.092	640	33	1.3524	16.0000	23.896
17		0.2305	3.2646	69.271	660	34	1.3876	16.0000	22.992
18		0.2324	3.2646	68.438	680	35	1.4237	16.0000	22.123
19		0.2342	3.2645	67.651	700	36	1.4596	16.0000	21.312
20	2 ∗	0.2362	4.1823	85.582	720	37	1.4966	16.0000	20.527
40	3 ∗	0.2721	5.1233	84.788	740	38	1.5318	16.0000	19.823
60	4 ∗	0.3080	6.0529	83.177	760	39	1.5677	16.0000	19.146
80	5 ∗	0.3442	7.0285	81.764	780	40	1.6045	16.0000	18.491
100	6 ∗	0.3801	8.2411	82.587	800	41	1.6392	16.0000	17.907
120	7 ∗	0.4159	9.5217	83.383	820	42	1.6759	16.0000	17.323
140	8 ∗	0.4520	10.7267	82.919	840	43	1.7123	16.0000	16.773
160	9 ∗	0.4881	12.0153	82.766	860	44	1.7474	16.0000	16.270
180	10 ∗	0.5240	13.4099	83.041	880	45	1.7841	16.0000	15.771
200	11 ∗	0.5600	14.8241	83.097	900	46	1.8190	16.0000	15.319
220	12	0.5959	16.0000	81.695	920	47	1.8559	16.0000	14.864
240	13	0.6320	16.0000	74.791	940	48	1.8921	16.0000	14.440
260	14	0.6680	16.0000	68.827	960	49	1.9273	16.0000	14.046
280	15	0.7041	16.0000	63.614	980	50	1.9655	16.0000	13.639
300	16	0.7400	16.0000	59.039	999	50	1.9986	16.0000	13.301

APPENDIX B: FURTHER INVESTIGATIONS OF PARTICLE STABILITY

B1 Longitude of ascending node

In addition to variations in particle inclination β and eccentricity e, we explore variations in the longitude of ascending node Ω. A particle can become misaligned with the Laplace surface if Ω moves out of the Laplace plane (or, synonymously, if its angular momentum vector moves out of the plane spanned by the planet's orbit angular momentum and spin vectors).

In Fig. B1 we show the Ω evolution of all stable and unstable particles in the $e_p = 0$, $\beta_p = 50°$ integration. The vast majority of particles lie near the Laplace surface's longitude of ascending node ($\Omega = -\pi/2$), while the unstable particles do exhibit non-trivial deviations from $\Omega = -\pi/2$. The number density in the bottom panel of Fig. B1 falls off with time, and the x-axis only extends to 7 Myr instead of the fully 16 Myr, because we performed the integrations for a fixed number of orbits. This corresponds to less physical time for the innermost particles, which are also the (ivection) unstable particles in this case. We have verified that the other five integrations have similar results.

B2 Ivection-unstable regions

Fig. B2 examines the full inclination dependence $\beta(r)$ of the disc regions susceptible to ivection resonance, examining the inner regions ($r < 0.6\,r_L$) of the unstable regions in Figs 4 and 5. Particles with smaller semimajor axis r tend to have larger β excitations than large r values (save for the $\beta_p = 80°$ integration), with particles near $r \approx 0.2\,r_L$ excited to retrograde inclinations ($\beta \approx 180° - \beta_p$). We speculate the r dependence of the β excitation is related to the test particle's proximity to the ivection (and possibly eviction; Touma & Wisdom 1998) resonance location(s). It is not clear to the authors why the $\beta_p = 80°$ integration has β excitations which do not seem to depend on r.

Fig. B3 presents a preliminary exploration into *why* there is a variation in inclination excitation amongst the ivection-unstable particles. For the three $e_p = 0.5$ integrations (Fig. 5), we plot test particle inclination as a function of initial β deviation from the Laplace surface, and as a function of initial eccentricity. The results for the three $e_p = 0$ integrations look virtually identical.

The stable and unstable distribution of particles in the right-hand column of Fig. B3 are very similar, suggesting little or no dependence of inclination excitation on eccentricity. In other words, a higher
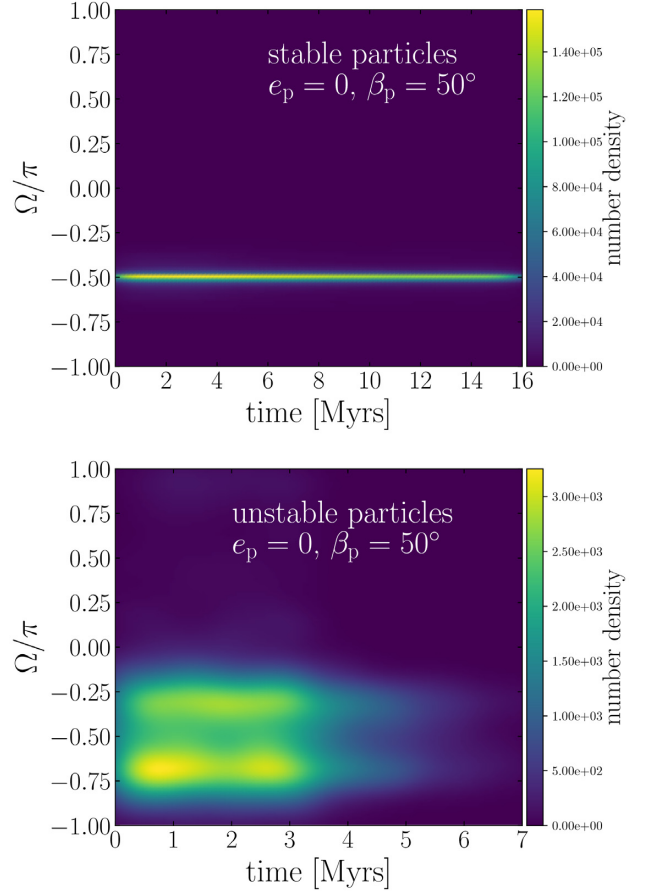

Figure B1. Evolution of test particle longitude of ascending node Ω of stable (top panel) and unstable (bottom panel) particles, from the $\beta_p = 50°$, $e_p = 0$ integration (middle row of Fig. 4). The vast majority of stable test particle Ω values lie close to the Laplace surface's longitude of ascending node $\Omega = -\pi/2$.

initial eccentricity does not improve a particle's chance of becoming unstable and undergoing ivection resonance.

The unstable particles in the left-hand column of Fig. B3, however, tend to be distributed $\gtrsim 0.5°$ away from 0 (above or below the Laplace surface). The stable particles in this same column, particularly those at large semimajor axes (shown in blue) display a linear dependence of $|\Delta\beta|$ on the initial β deviation due to nodal precession from the host star's tidal torque.
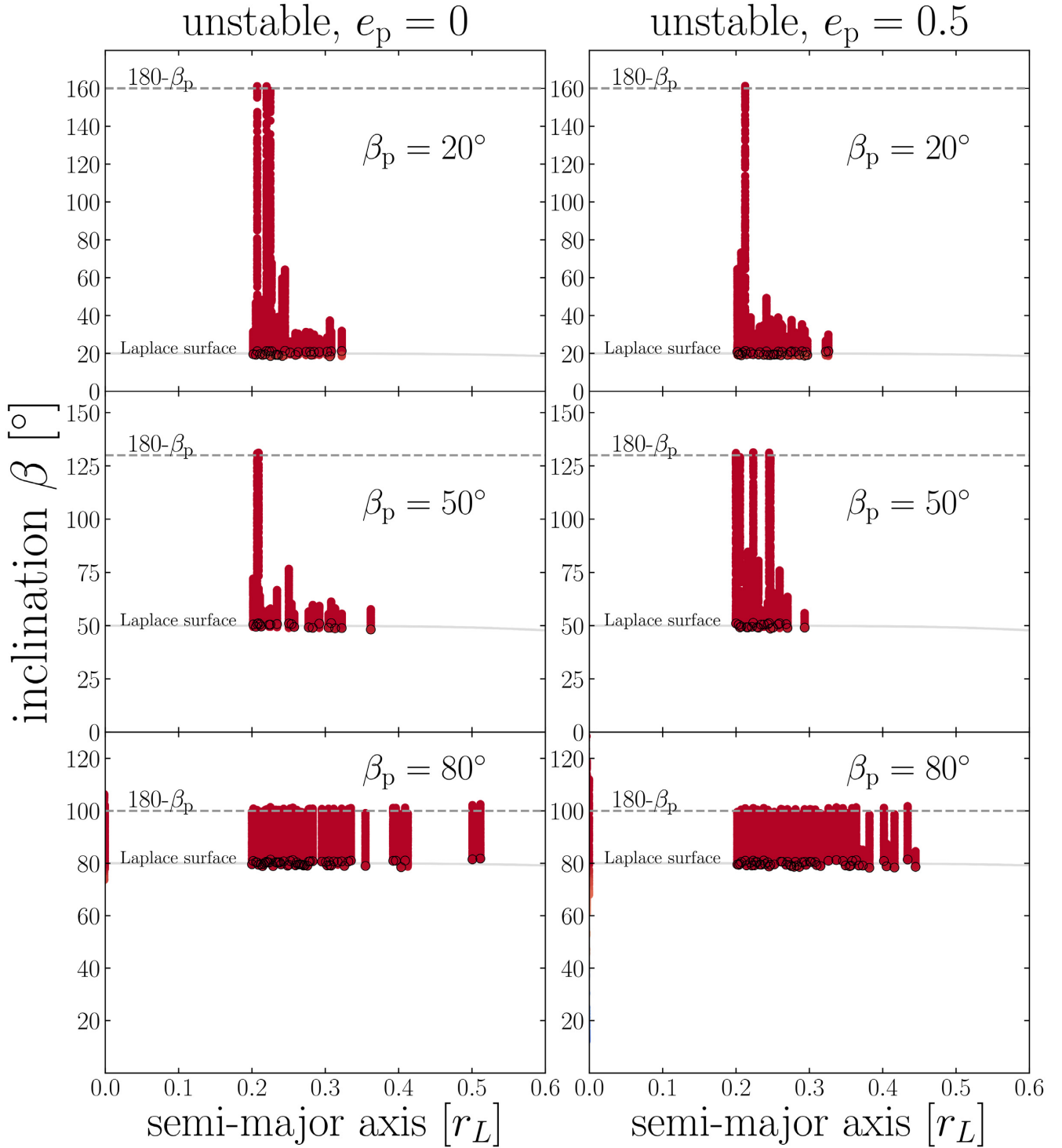
Figure B2. The inclinations β of unstable particles in Fig. 4 (left-hand panels) and Fig. 5 (right-hand panels), focusing on the inner regions of the disc susceptible to ivection instability ($r < 0.6\,r_{\mathrm{L}}$). The full range of β values are displayed, alongside the Laplace surface inclination β_{p} (solid grey line) and $180° - \beta_{\mathrm{p}}$ (dashed grey line). All particles have negligible eccentricity over the course of the integration ($e[t] \lesssim 0.01$).
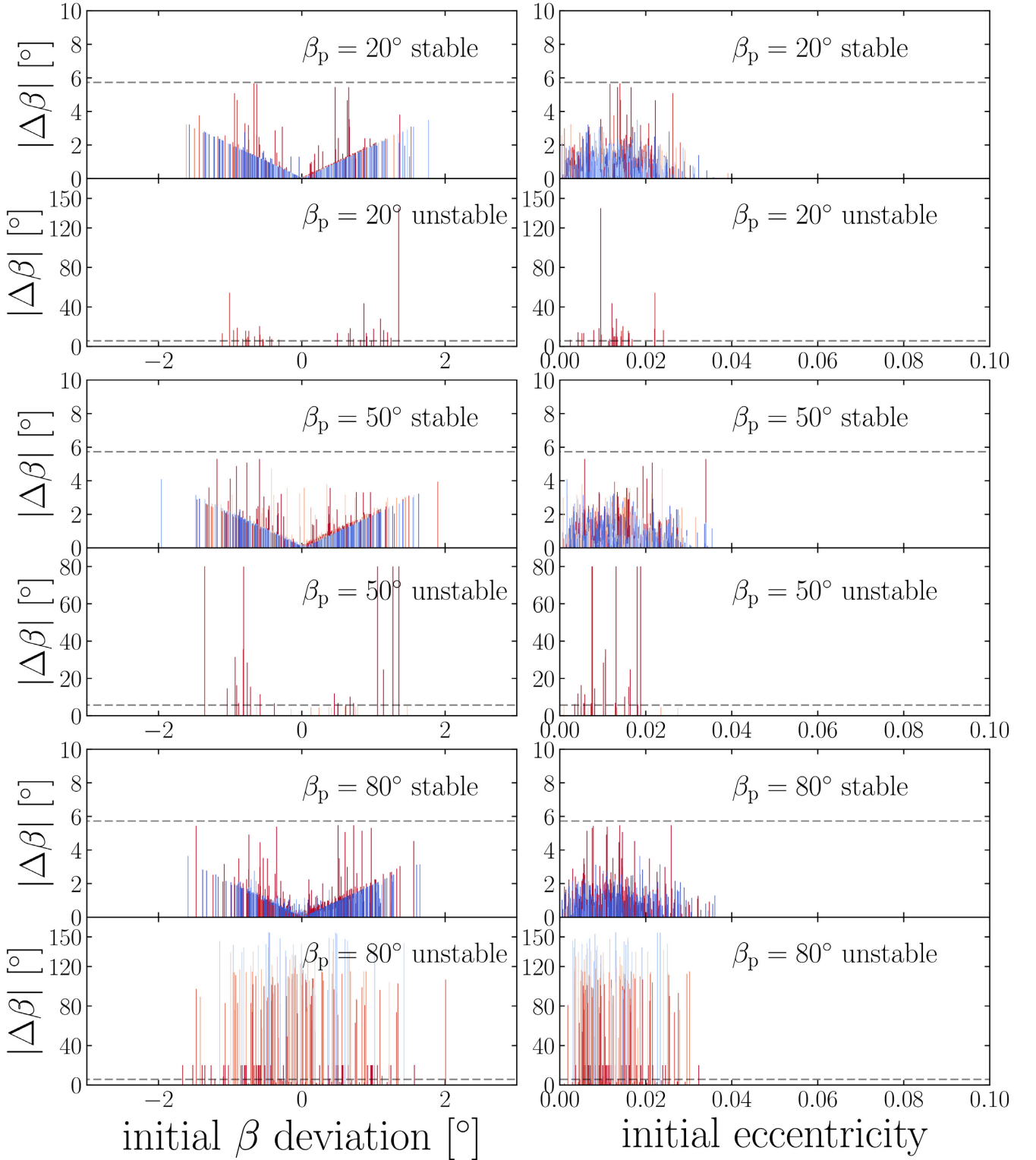
Figure B3. Maximum particle inclination excitation $|\Delta\beta|$ as a function of initial inclination deviation and initial eccentricity for the three $e_p = 0.5$ integrations (see Fig. 5). An initial β deviation of $0°$ and e of 0 corresponds to a particle initialized directly on the Laplace surface. In all panels, the horizontal dashed grey line corresponds to the stability condition $|\Delta\beta| = |\beta[t] - \beta[0]| < 0.1$ rad $= 5.73°$.

This paper has been typeset from a TEX/LATEX file prepared by the author.